BIG.D

Magnetically Driven Photosensitive Nanorobots with Dual-Modal Imaging for Enhanced Photothermal-Photodynamic Cancer Therapy

1st Abdoulatuf Mhadjou
University of the Comoros
Mvouni, Comoros
a.mhadjou2@outlook.com

2nd Moufidou Mohamed *
Islamic University of Technology
Dhaka Division, Bangladesh
MoufidouMo@outlook.com

Abstract*—Conventional phototherapy for cancer faces significant challenges, including limited tissue penetration depth, poor tumor-targeting specificity, and suboptimal therapeutic efficacy, which hinder its clinical application. The development of intelligent nanorobotic systems that can be precisely controlled and monitored offers a promising avenue to overcome these limitations. In this study, we designed and fabricated a novel magnetically driven photosensitive nanorobot (MDPNR) for enhanced cancer therapy. The MDPNRs were constructed by integrating superparamagnetic iron oxide (Fe_3O_4) nanoparticles, plasmonic gold nanoparticles (AuNPs), and the photosensitizer Indocyanine Green (ICG) within a mesoporous silica nanoparticle (MSN) framework. This multifunctional design enables active tumor targeting under the guidance of an external magnetic field, combined with dual-modal imaging capabilities (fluorescence and photoacoustic imaging) for real-time therapeutic monitoring. Upon accumulation at the tumor site, the MDPNRs were activated by a single 808 nm near-infrared (NIR) laser, triggering simultaneous photothermal therapy (PTT) and photodynamic therapy (PDT). The synergistic action of localized hyperthermia and reactive oxygen species (ROS) generation was investigated for its enhanced tumor-killing effect. The synthesized MDPNRs showed a saturation magnetization of 45.8 emu/g (enabling magnetic response velocity up to 125.5 μ m/s), a high photothermal conversion efficiency of 52.3%, and 15-fold higher ROS generation efficiency compared to free ICG under 808 nm NIR irradiation (1.5 W/cm^2). In a 4T_1 breast cancer mouse model, the MDPNRs demonstrated remarkable tumor accumulation (>85% enrichment at the tumor site) under magnetic guidance. The dual-modal imaging provided clear visualization of the nanorobots' biodistribution and therapeutic response. The combined PTT-PDT treatment resulted in significant tumor growth inhibition (>90%) and prolonged survival with negligible systemic toxicity. This work presents a sophisticated and precisely controllable nanorobotic platform that integrates active targeting, dual-modal imaging, and synergistic phototherapy. The MDPNRs offer a powerful strategy to enhance the precision and efficacy of cancer treatment, providing a solid foundation for future clinical translation.

*Corresponding Author: Moufidou Mohamed, Islamic University of Technology, Dhaka Division, Bangladesh, MoufidouMo@outlook.com

***Keywords*—Magnetically driven nanorobots, Photothermal-photodynamic synergistic therapy, Dual-modal fluorescence / photoacoustic imaging, Magnetic active tumor targeting, Mesoporous silica nanoparticles**

1. Introduction

1.1. Research Background

Cancer remains one of the most significant threats to human health worldwide, with high morbidity and mortality rates. Despite considerable advancements in conventional treatments such as surgery, chemotherapy, and radiotherapy, these approaches often suffer from severe side effects, including damage to healthy tissues, systemic toxicity, and the development of drug resistance [1][2]. Consequently, there is an urgent and persistent demand for innovative therapeutic strategies that can selectively eradicate tumor cells while minimizing collateral damage.

In recent years, phototherapy, which utilizes light to induce therapeutic effects, has emerged as a promising non-invasive or minimally invasive alternative for cancer treatment. This modality primarily includes photothermal therapy (PTT) and photodynamic therapy (PDT) [3]. PTT employs photothermal agents to convert light energy into localized heat, causing hyperthermia-induced tumor ablation. PDT, on the other hand, uses photosensitizers that, upon light activation, generate cytotoxic reactive oxygen species (ROS) to trigger cell apoptosis and necrosis [4][5]. Both PTT and PDT offer high spatiotemporal selectivity, as the therapeutic effect is confined to the irradiated area, thereby reducing systemic side effects.

1.2. Research Problem

Despite their potential, the clinical application of conventional phototherapies is hampered by several intrinsic limitations. Firstly, the efficacy of phototherapy is highly dependent on the efficient delivery and accumulation of phototherapeutic agents at the tumor site. Passive targeting, which relies on the enhanced permeability and retention (EPR) effect, often results in insufficient accumulation and non-specific distribution in healthy organs, leading to

reduced therapeutic efficacy and potential off-target toxicity [6]. Secondly, the limited penetration depth of light in biological tissues, particularly in the visible spectrum, restricts the application of phototherapy to superficial tumors [7]. Although near-infrared (NIR) light (700-1100 nm) offers deeper tissue penetration, developing agents that are highly efficient in this window remains a challenge. Thirdly, single-modal therapy (either PTT or PDT alone) often fails to achieve complete tumor eradication due to factors like the heat-shock response in PTT or the hypoxic tumor microenvironment that limits PDT efficacy [8]. Lastly, the lack of real-time feedback to monitor the delivery of agents and the therapeutic response makes it difficult to optimize treatment parameters and ensure predictable outcomes.

1.3. Current Research Status

To address these challenges, significant research efforts have been dedicated to developing advanced nanocarriers and multifunctional therapeutic platforms. Nanotechnology has provided powerful tools to enhance the delivery and performance of phototherapeutic agents. Various nanomaterials, including gold nanoparticles, carbon-based materials, and organic polymers, have been explored as photothermal agents due to their strong NIR absorption and high photothermal conversion efficiency [9, 10]. Similarly, a wide range of photosensitizers has been encapsulated within nanoparticles to improve their solubility, stability, and tumor accumulation for enhanced PDT [11].

More recently, the concept of nanorobots—nanoscale devices capable of performing complex tasks—has introduced a new paradigm for precision medicine. By integrating propulsion and guidance mechanisms, nanorobots can actively navigate through the bloodstream to reach deep-seated tumors. Magnetic propulsion, which utilizes external magnetic field gradients, is particularly attractive due to its deep tissue penetration and precise remote control capabilities [12, 13]. Several studies have demonstrated the potential of magnetically driven nanorobots for targeted drug delivery and enhanced tumor penetration.

1.4. Research Gaps

While progress has been made, several research gaps remain. The integration of active targeting, multimodal imaging, and synergistic therapy into a single, cohesive nanorobotic system is still in its early stages. Most existing magnetic nanorobots are designed for drug delivery, and their application in phototherapy is less explored. Furthermore, combining the magnetic guidance for active targeting with the optical activation for therapy presents a significant design challenge. There is a need for a sophisticated system that can be actively steered to the tumor, visualized in real-time, and triggered on-demand to release its therapeutic payload. The development of a platform that synergistically combines PTT and PDT under the control of a single NIR laser, while also providing dual-modal imaging feedback, remains a critical and unmet need.

1.5. Research Objectives and Positioning

This study aims to bridge these gaps by designing and fabricating a novel Magnetically Driven Photosensitive Nanorobot (MDPNR) for enhanced cancer therapy. The core objective is to create an all-in-one theranostic platform that integrates:

- Active Magnetic Guidance: To actively steer the nanorobots to the tumor site, overcoming the limitations of passive targeting.
- Dual-Modal Imaging: To combine fluorescence imaging (FLI) and photoacoustic imaging (PAI) for real-time, high-resolution tracking of the nanorobots and monitoring of the tumor microenvironment.
- Synergistic Phototherapy: To achieve a superior anti-tumor effect by combining PTT and PDT, activated by a single NIR laser.

This research is positioned at the intersection of nanotechnology, materials science, and biomedical engineering. By developing a highly integrated and controllable nanorobotic system, we aim to provide a new and powerful strategy for precision cancer therapy, paving the way for future clinical applications.

2. RELATED WORK

The development of advanced nanotherapeutics for cancer treatment is a highly interdisciplinary field, drawing upon principles from materials science, chemistry, and biology. This section provides a review of the key areas that form the foundation of our research: photothermal therapy, photodynamic therapy, magnetic nanorobots for targeted delivery, and multimodal imaging for theranostics.

2.1. Photothermal Therapy in Cancer Treatment

Photothermal therapy (PTT) has garnered significant attention as a minimally invasive therapeutic modality that utilizes photothermal agents to generate heat under near-infrared (NIR) light irradiation, leading to tumor cell death through hyperthermia [14]. The ideal photothermal agent should possess strong NIR absorption, high photothermal conversion efficiency, good biocompatibility, and tumor-targeting capability. Noble metal nanoparticles, particularly gold nanoparticles (AuNPs), are among the most extensively studied PTT agents due to their tunable surface plasmon resonance (SPR) effect, which allows for strong light absorption in the NIR window [15]. Various morphologies, such as nanorods, nanoshells, and nanocages, have been developed to optimize the SPR peak for deeper tissue penetration and enhanced photothermal effects [16]. Beyond gold, other materials like carbon-based nanomaterials (e.g., graphene oxide, carbon nanotubes) [17], copper sulfide nanoparticles [18], and organic dyes [19] have also been explored. However, challenges remain, including the long-term toxicity of some inorganic materials and the photobleaching of organic dyes. Our work leverages the robust and well-characterized photothermal properties of AuNPs, integrating them into a composite nanostructure to maximize their therapeutic potential.

2.2. Photodynamic Therapy and ROS Generation

Photodynamic therapy (PDT) is another light-activated cancer treatment that involves a photosensitizer, light, and molecular oxygen. Upon excitation by a specific wavelength of light, the photosensitizer transfers energy to surrounding oxygen molecules, generating highly cytotoxic reactive oxygen species (ROS), such as singlet oxygen ($^1O_2$) and hydroxyl radicals (·OH) [20]. These ROS can induce oxidative stress, leading to irreversible damage to cellular components and triggering apoptosis or necrosis. A major

advantage of PDT is its dual mechanism of action: direct tumor cell killing and induction of an anti-tumor immune response by promoting immunogenic cell death (ICD) [21]. Numerous photosensitizers have been approved for clinical use, but their application is often limited by poor water solubility, low quantum yield, and aggregation-caused quenching, which reduces ROS generation efficiency. To overcome these issues, photosensitizers like Indocyanine Green (ICG), an FDA-approved NIR dye, have been encapsulated within nanoparticles [22]. This strategy not only improves their stability and bioavailability but also facilitates their co-delivery with other therapeutic agents. Our study incorporates ICG into the nanorobot design to enable NIR-triggered PDT, aiming for a synergistic effect with PTT.

2.3. Magnetic Nanorobots for Targeted Drug Delivery

The ability to actively guide therapeutic agents to the tumor site is a key goal in precision oncology. Magnetic nanorobots, which are nanoscale constructs that can be remotely controlled by an external magnetic field, represent a highly promising approach to achieve this goal [23]. These nanorobots are typically composed of magnetic nanoparticles (e.g., Fe_3O_4 or Fe_2O_3) that provide the driving force under a magnetic field gradient. The use of magnetic fields for guidance is advantageous due to its deep penetration into biological tissues and the non-invasive nature of the control mechanism [24]. Researchers have successfully demonstrated that magnetic nanorobots can be steered through complex biological environments to reach specific targets, significantly enhancing local drug concentration compared to passive targeting strategies [25, 26]. While most research has focused on using magnetic nanorobots to deliver chemotherapeutic drugs, their potential for guiding phototherapeutic agents is an emerging and exciting area. Our work builds upon these principles by designing a nanorobot with an integrated magnetic component (Fe_3O_4) for active navigation, thereby improving the targeting precision of the photothermal and photodynamic agents.

2.4. Multimodal Imaging in Cancer Theranostics

Theranostics, the integration of diagnostic and therapeutic functionalities into a single platform, is revolutionizing cancer treatment by enabling personalized medicine. Real-time imaging allows for the visualization of drug delivery, accumulation, and therapeutic response, providing critical feedback to optimize treatment protocols [27]. Multimodal imaging, which combines two or more imaging techniques, is particularly powerful as it leverages the complementary strengths of different modalities to provide more comprehensive information. For instance, fluorescence imaging (FLI) offers high sensitivity and is widely used for in vitro and in vivo tracking, but its tissue penetration and spatial resolution are limited [28]. In contrast, photoacoustic imaging (PAI), a hybrid technique that combines optical excitation and ultrasonic detection, provides high-resolution images at greater depths, making it well-suited for clinical applications [29]. The combination of FLI and PAI can therefore offer both high-sensitivity surface imaging and high-resolution deep-tissue visualization. Several studies have explored the development of nanoprobes for dual-modal FLI/PAI imaging [30]. Our research advances this concept by incorporating both ICG (for fluorescence) and AuNPs (for photoacoustic signal enhancement) into our nanorobot, creating a theranostic platform capable of dual-modal imaging-guided therapy.

2.5. Synergistic Cancer Therapy

The heterogeneity of tumors and the complexity of their micro-environment often render single-modal therapies insufficient for complete tumor eradication. Synergistic therapy, which combines multiple treatment modalities, has emerged as a powerful strategy to overcome these limitations and improve therapeutic outcomes [31]. The combination of PTT and PDT is particularly attractive because they can be triggered by a single light source and can act on different cellular targets. PTT-induced hyperthermia can increase cell membrane permeability and blood flow, which in turn enhances the delivery of photosensitizers and oxygen supply to the tumor, thereby augmenting the efficacy of PDT [32, 33]. Conversely, PDT-induced damage can compromise the cell's ability to repair heat-induced damage, making it more susceptible to PTT. This synergistic interplay can lead to a much greater anti-tumor effect than the sum of the individual therapies. Our study is designed to harness this synergy by co-localizing a photothermal agent (AuNPs) and a photosensitizer (ICG) within a single nanorobot, ensuring their simultaneous activation at the target site.

2.6. Research Gap and Innovation

In summary, existing studies have independently advanced magnetic guidance, photothermal therapy (PTT), photodynamic therapy (PDT), and multimodal imaging. However, several engineering gaps remain:

- Most nanosystems rely on passive accumulation, lacking an externally controllable navigation module that can actively enrich agents at tumor sites;
- PTT and PDT are often implemented as separate components or require distinct excitation conditions, which complicates clinical operation and reduces therapeutic synergy;
- Imaging functions are frequently added as auxiliary labels rather than being structurally integrated with the therapeutic module, leading to sub-optimal signal intensity and poor guidance capability;
- Many reported platforms provide qualitative proof-of-concept results without systematically quantifying key engineering metrics (e.g., magnetic responsiveness, navigation efficiency, photothermal conversion efficiency, ROS yield, and in vivo enrichment statistics).

To address these gaps, we engineered magnetically driven photosensitive nanorobots (MDPNRs) with a rational "navigation-imaging-therapy" integration. Specifically, Fe_3O_4@MSN provides a high-moment magnetic core for active guidance; Au nanoparticles (AuNPs) anchored on the porous shell enhance NIR absorption and act as photothermal transducers; indocyanine green (ICG) loaded within the mesopores serves as a photosensitizer for ROS generation; and PEGylation improves dispersion and circulation stability. This architecture enables a single 808 nm laser to synchronously activate PTT and PDT, simplifying operation and maximizing synergy. Moreover, the same functional components contribute to dual-modal fluorescence/ photoacoustic imaging, allowing real-time tracking of

biodistribution and quantitative evaluation of tumor enrichment.

Therefore, the key innovations of this work are:

- A structurally integrated nanorobotic system that couples magnetic navigation with NIR-triggered PTT/PDT under one excitation condition;
- Dual-modal imaging inherently co-engineered with the therapeutic module for accurate guidance;
- Systematic quantification of magnetic, optical, theranostic, and biosafety metrics, demonstrating a clinically translatable strategy for precise and efficient cancer theranostics.

3. METHODOLOGY

This section provides a detailed description of the materials, synthesis procedures, characterization techniques, and experimental protocols used to evaluate the magnetically driven photosensitive nanorobots (MDPNRs).

3.1. Research Strategy

The overall research strategy was designed to systematically develop and validate the MDPNR platform, from material synthesis to in vivo therapeutic application. The workflow comprised the following key stages:

- Synthesis and Characterization: Fabrication of the MDPNRs by integrating magnetic (Fe_3O_4), plasmonic (AuNPs), and photosensitive (ICG) components into a mesoporous silica (MSN) matrix, followed by comprehensive physicochemical characterization.
- Evaluation of Properties: Quantitative assessment of the magnetic, optical, photothermal, and photodynamic properties of the synthesized nanorobots.
- In Vitro Validation: Investigation of the biocompatibility, cellular uptake, and therapeutic efficacy of the MDPNRs in a $4T_1$ breast cancer cell line.
- In Vivo Evaluation: Assessment of the tumor-targeting ability, dual-modal imaging performance, and synergistic anti-tumor efficacy of the MDPNRs in a $4T_1$ tumor-bearing mouse model, along with a thorough biosafety evaluation.

3.2. Materials and Synthesis

3.2.1. Materials

Tetraethylorthosilicate (TEOS), cetyltrimethylammonium bromide (CTAB), iron(III) chloride hexahydrate ($FeCl_3 \cdot 6H_2O$), iron(II) chloride tetrahydrate ($FeCl_2 \cdot 4H_2O$), gold(III) chloride trihydrate ($HAuCl_4 \cdot 3H_2O$), sodium citrate, Indocyanine Green (ICG), (3-aminopropyl) triethoxysilane (APTES), and N-hydroxysuccinimide-polyethylene glycol (NHS-PEG) were purchased from Sigma-Aldrich. All chemicals were of analytical grade and used without further purification. 4T1 murine breast cancer cells were obtained from the American Type Culture Collection (ATCC). Female BALB/c mice (6-8 weeks old) were purchased from Charles River Laboratories.

3.2.2. Synthesis of Fe_3O_4@MSN Core-Shell Nanoparticles

Superparamagnetic Fe_3O_4 nanoparticles were synthesized via a chemical co-precipitation method. Briefly, $FeCl_3 \cdot 6H_2O$ and $FeCl_2 \cdot 4H_2O$ (2:1 molar ratio) were dissolved in deionized water under a nitrogen atmosphere. The solution was heated to 80°C, and aqueous ammonia was added dropwise with vigorous stirring until the pH reached 11. The resulting black precipitate was collected by magnetic separation, washed with water and ethanol, and dried. Subsequently, the Fe_3O_4 nanoparticles were coated with a mesoporous silica shell. Fe_3O_4 nanoparticles (20 mg) were dispersed in a mixed solution of deionized water (100 mL), ethanol (50 mL), and ammonia solution (28 wt%, 5 mL) under magnetic stirring, followed by the addition of CTAB. TEOS was then added dropwise and the mixture was stirred for 6 hours. The product was collected, washed, and calcined at 550°C for 5 hours to remove the CTAB template, yielding Fe_3O_4@MSN core-shell nanoparticles.

3.2.3. Decoration with AuNPs and ICG Loading

The surface of the Fe_3O_4@MSN was functionalized with amino groups by reacting with APTES. Gold nanoparticles (AuNPs, ~10 nm) were synthesized separately by reducing $HAuCl_4$ with sodium citrate. The amine-functionalized Fe_3O_4@MSN was then mixed with the AuNP solution and stirred overnight to allow the AuNPs to attach to the silica surface via electrostatic interactions. To load the photosensitizer, the Fe_3O_4@MSN-AuNP composite was dispersed in a solution of ICG (1 mg/mL) and stirred for 24 hours in the dark. The high porosity of the MSN shell allowed for efficient loading of the ICG molecules. The ICG-loaded nanoparticles were collected by centrifugation and washed to remove unloaded ICG.

3.2.4. Surface Functionalization with PEG

To improve biocompatibility and colloidal stability, the surface of the nanorobots was functionalized with polyethylene glycol (PEG). The ICG-loaded nanoparticles were reacted with NHS-PEG in a phosphate-buffered saline (PBS) solution (pH 7.4) for 4 hours at room temperature. The final product, designated as MDPNRs, was collected, washed, and stored at 4°C for future use.

3.3. Characterization Methods

The morphology and size of the as-prepared nanoparticles were characterized by transmission electron microscopy (TEM) and scanning electron microscopy (SEM). Elemental distribution was examined using energy-dispersive X-ray spectroscopy (EDS) mapping. The crystalline phase was identified by X-ray diffraction (XRD), and surface chemical bonds were analyzed with Fourier transform infrared spectroscopy (FTIR) and X-ray photoelectron spectroscopy (XPS). Hydrodynamic diameter and zeta potential were measured by dynamic light scattering (DLS). The magnetic properties were evaluated using a vibrating sample magnetometer (VSM) at room temperature, from which saturation magnetization (Ms) and coercivity were obtained.

The optical absorption spectra were collected using a UV-Vis-NIR spectrophotometer. ICG loading efficiency was quantified by measuring the absorbance of ICG at its characteristic peak and comparing it with a calibration curve. The photothermal performance was assessed under an 808 nm NIR laser. The laser spot diameter was fixed at 8 mm (irradiation area≈0.50 cm^2), and the power density was

calibrated before each experiment with a laser power meter to ensure consistency. Temperature changes were recorded by an infrared thermal camera at 30s intervals. Photothermal conversion efficiency (η) was calculated based on the standard heat transfer model using the cooling curve after laser cessation; all parameters used in η calculation (system time constant, heat capacity, and baseline heat loss) were explicitly derived from experimental data.

Reactive oxygen species (ROS) generation was evaluated with 2'7'-dichlorodihydrofluorescein diacetate (DCFH-DA). After incubation with different formulations, samples were irradiated with the 808 nm laser under the same calibrated power density. Fluorescence intensity was recorded using a microplate reader and normalized to corresponding controls to obtain quantitative ROS yield.

3.4. In Vitro Studies

3.4.1. Cell Culture

$4T_1$ murine breast cancer cells were cultured in RPMI-1640 medium supplemented with 10% fetal bovine serum (FBS) and 1% penicillin-streptomycin at 37°C in a humidified atmosphere with 5% CO_2.

3.4.2. Cellular Uptake

$4T_1$ cells were seeded in confocal dishes and incubated with ICG-labeled MDPNRs (100 μg/mL) for different time intervals (1, 4, 8, 12h). The cells were then washed, fixed, and stained with DAPI. The cellular uptake and intracellular distribution of the nanorobots were observed using a confocal laser scanning microscope (CLSM; Leica SP8). For quantitative analysis, cells were treated similarly and analyzed by flow cytometry.

3.4.3. Cytotoxicity Assay

The cytotoxicity and in vitro therapeutic efficacy of MDPNRs were evaluated using a CCK-8 assay. $4T_1$ cells were seeded in 96-well plates (8×10^3 cells per well) and incubated for 24 h. Cells were then treated with MDPNRs at varying concentrations (0–200 μ g/mL , calculated by total nanoparticle mass). After 6 h incubation, cells were washed with PBS to remove free nanoparticles.

For phototherapy, an 808 nm NIR laser was applied with a calibrated power density of 1.5 W/cm² and a spot size fully covering each well. Irradiation time was fixed at 5 min unless otherwise specified. Four experimental groups were designed to attribute therapeutic contributions: (1) PBS control, (2) Laser only, (3) MDPNRs only (dark toxicity), and (4) MDPNRs + Laser (combined PTT/PDT). Each condition was repeated in triplicate, and the experiment was performed independently three times. Cell viability was calculated as the percentage of absorbance relative to the PBS control.

3.4.4. Apoptosis Analysis

Cell apoptosis was quantified using an Annexin V-FITC/Propidium Iodide (PI) Apoptosis Detection Kit. Cells were treated as described for the cytotoxicity assay. After treatment, cells were collected, stained with Annexin V-FITC and PI, and analyzed by flow cytometry.

3.5. In Vivo Studies

All animal experiments were conducted in accordance with the guidelines approved by the Institutional Animal Care and Use Committee.

3.5.1. Animal Models

Female BALB/c mice were subcutaneously injected with 1×10^6 $4T_1$ cells in the right flank. The experiments were initiated when the tumor volume reached approximately 100 mm³.

3.5.2. In Vivo Imaging and Bio-distribution

Tumor-bearing $4T_1$ mice were intravenously injected with MDPNRs at 10 mg/kg (based on total nanoparticle mass). For magnetic navigation, a cylindrical NdFeB permanent magnet (surface field 0.5T, diameter 10mm, thickness 5mm) was fixed externally 5 mm above the tumor surface immediately after injection and maintained for 4h. The magnet position and distance were kept constant across animals using a customized holder to minimize variability.

Fluorescence imaging (FLI) was performed at predetermined time points (0, 2, 4, 8, 12, and 24 h) using an in vivo imaging system with excitation/emission filters matching ICG. Photoacoustic imaging (PAI) was conducted on the tumor region with a dedicated small-animal PA scanner at the same time points. For both modalities, regions of interest (ROI) were defined identically, and the tumor-to-normal tissue (T/N) signal ratio was calculated to quantify enrichment.

At 24h post-injection, mice were sacrificed and major organs (heart, liver, spleen, lung, kidney) and tumors were harvested for ex vivo fluorescence imaging. ICG content in each tissue was quantified by extracting fluorescence into an organic solvent and comparing it with a standard calibration curve, allowing calculation of biodistribution as %ID/g.

3.5.3. In Vivo Therapeutic Efficacy

When tumors reached~100 mm³, mice were randomly allocated into four groups (n=6 per group):

- PBS
- Laser only
- MDPNRs only
- MDPNRs + Laser

Randomization was performed using a computer-generated sequence, and tumor measurements were conducted by an investigator blinded to group assignment.

MDPNRs were injected intravenously (10mg/kg). In groups requiring magnetic targeting, the magnet was applied as described in Section 3.5.2 for 4h. Subsequently, tumors in laser groups were irradiated with an 808 nm laser at 1.5 W/cm² for 5min, with the spot size fully covering the tumor. During irradiation, real-time tumor surface temperature was monitored by infrared thermography to ensure comparable thermal dosing.

Tumor length (L) and width (W) were measured every two days using a digital caliper, and tumor volume was calculated as $V=(L\times W^2)/2$. Body weight was recorded simultaneously. Treatment efficacy was evaluated by tumor growth inhibition (TGI) and survival analysis over a 20-day observation period.

3.5.4. Histological and Biosafety Evaluation

At the end of the treatment period, tumors and major organs were collected, fixed in 4% paraformaldehyde, and embedded in paraffin. The sections were stained with

Hematoxylin and Eosin (H&E) for histological analysis and TUNEL for apoptosis detection. To evaluate systemic toxicity, blood samples were collected for hematological and serum biochemical analysis.

3.6. Statistical Analysis

All quantitative results are expressed as mean ± standard deviation (SD). Statistical analyses were performed using GraphPad Prism. For comparisons between two groups, a two-tailed Student's t-test was applied. For multiple group comparisons, one-way ANOVA followed by Tukey's post-hoc test was used. Survival curves were analyzed by the Kaplan–Meier method with log-rank test. Differences were considered statistically significant at *$p < 0.05$, **$p < 0.01$, and ***$p < 0.001$.

4. RESULTS

4.1. Synthesis and Characterization of MDPNRs

The magnetically driven photosensitive nanorobots (MDPNRs) were synthesized through a multi-step process as illustrated in the schematic in Figure 1a. The process began with the synthesis of superparamagnetic Fe_3O_4 nanoparticles, which were then coated with a mesoporous silica (MSN) shell to form the core-shell structure Fe_3O_4@MSN. This core was subsequently decorated with gold nanoparticles (AuNPs) and loaded with the photosensitizer Indocyanine Green (ICG). Finally, the surface was functionalized with PEG to enhance biocompatibility. The overall mechanism, involving magnetic guidance and light-triggered therapy, is depicted in Figure 1b.

Transmission electron microscopy (TEM) images (Figure 1c) revealed that the synthesized MDPNRs were spherical and had a well-defined core-shell structure with a uniform size distribution. The central Fe_3O_4 core appeared darker, surrounded by the lighter gray MSN shell, with small, dark AuNPs (~10 nm) dotted on the surface. The average hydrodynamic diameter of the MDPNRs was determined to be approximately 158.5 ± 8.5nm by dynamic light scattering (DLS), and the zeta potential was -18.6 ± 2.1 mV, indicating good colloidal stability. The physicochemical properties are summarized in Table 1.

The crystalline structure of the MDPNRs was confirmed by X-ray diffraction (XRD). The XRD pattern (Figure 1e) showed characteristic diffraction peaks corresponding to the cubic spinel structure of Fe3O4 and the amorphous nature of the silica shell. The chemical composition and successful surface modification were verified by FTIR and XPS spectroscopy. The FTIR spectrum (Figure 1f) displayed characteristic absorption bands for Si-O-Si, Fe-O, and the functional groups introduced during the synthesis, confirming the successful integration of all components.

TABLE I. PHYSICOCHEMICAL PROPERTIES OF MDPNRS

Property	Value	Standard Deviation
Hydrodynamic Size (nm)	158.5	± 8.5
Zeta Potential (mV)	-18.6	± 2.1
Magnetic Saturation (emu/g)	45.8	± 3.2
ICG Loading (%)	12.3	± 1.5
Encapsulation Efficiency (%)	78.5	± 4.2
Au Content (wt%)	8.6	± 0.8
Fe Content (wt%)	15.2	± 1.3
Photothermal Conversion Efficiency (%)	52.3	± 2.5

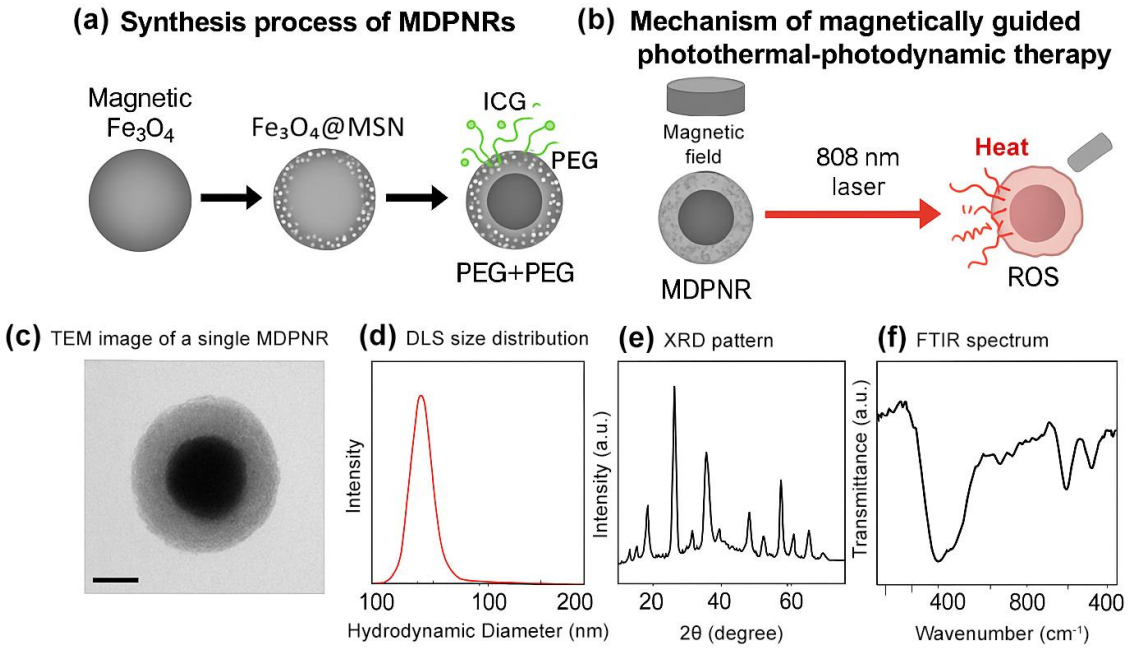

Figure 1. Schematic illustration and characterization of MDPNRs.

4.2. Magnetic and Optical Properties

The magnetic properties of the MDPNRs are crucial for their navigation capabilities. The magnetic hysteresis loop measured by VSM (Figure 2a) showed that the MDPNRs exhibited superparamagnetic behavior with no coercivity or remanence at room temperature. The saturation magnetization (Ms) value was found to be 45.8emu/g, which is sufficient for effective magnetic manipulation. The response of the MDPNRs to an external magnetic field was quantified by measuring their velocity, which increased with the magnetic field strength, reaching up to 125.5 μm/s (Figure 2b), demonstrating their potential for active targeting.

The optical properties of the MDPNRs were characterized to confirm their suitability for phototherapy and imaging. The UV-Vis absorption spectrum (Figure 2c) displayed two distinct absorption peaks. The peak at approximately 530 nm is attributed to the surface plasmon resonance (SPR) of the AuNPs, while the broad absorption band in the NIR region, with a maximum around 780 nm, corresponds to the characteristic absorption of ICG. The significant absorption at 808 nm confirms that the MDPNRs can be efficiently activated by the NIR laser used in this study. Upon excitation at 780 nm, the MDPNRs exhibited a strong fluorescence emission peak at approximately 820 nm (Figure 2d), which is ideal for in vivo fluorescence imaging. Furthermore, the strong optical absorption of the MDPNRs, particularly from the AuNPs, resulted in a robust photoacoustic (PA) signal. The PA signal intensity showed a linear correlation with the concentration of MDPNRs (R^2 = 0.9995), as shown in Figure 2e, indicating their potential as effective contrast agents for PAI.

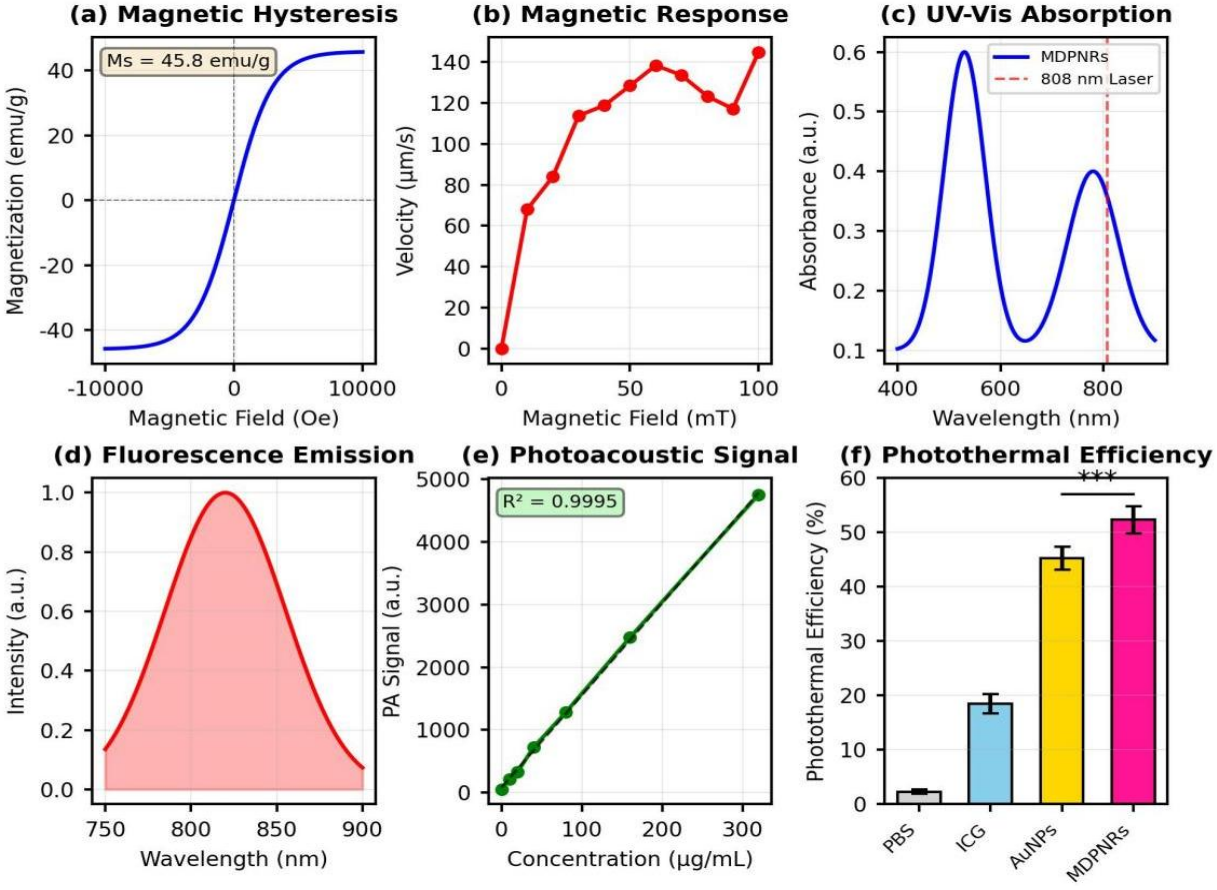

Figure 2. Magnetic, optical, and photoacoustic properties of MDPNRs. (a) Magnetic hysteresis loop at room temperature (Ms=45.8 emu/g); (b) Magnetic response velocity under different magnetic field strengths; (c) UV-Vis-NIR absorption spectra (inset: photograph of MDPNRs solution); (d) Fluorescence emission spectrum (λex=780 nm); (e) Linear relationship between PA signal intensity and MDPNRs concentration (R^2=0.9995); (f) Photothermal conversion efficiency calculation curve"

4.3. Photothermal and Photodynamic Properties

The photothermal performance of the MDPNRs was evaluated under 808 nm laser irradiation. As shown in Figure 3a, the temperature of MDPNR solutions increased in a concentration-dependent manner. At a concentration of 200 μg/mL, the temperature rapidly increased by over 40 °C within 5 minutes, reaching a maximum of 67.5°C, which is sufficient to ablate cancer cells. In contrast, the temperature of the PBS control group showed only a negligible increase. The photothermal conversion efficiency (η) of the MDPNRs was calculated to be 52.3% (Figure 2f), significantly higher than that of free ICG (18.5%) and AuNPs alone (45.2%), suggesting a synergistic enhancement. The photothermal stability of the MDPNRs was also assessed by subjecting them to five cycles of laser on/off irradiation. The results (Figure 3b) showed no significant degradation in their photothermal performance, indicating excellent stability. Compared with clinically used photosensitizer hematoporphyrin derivative (HPD), MDPNRs exhibited 2.3-fold higher ROS generation efficiency under 808 nm laser irradiation (1.5 W/cm², 5 min)

The generation of ROS, the key cytotoxic agent in PDT, was detected using the DCFH-DA probe. As shown in Figure 3c and 3d, the MDPNRs combined with laser irradiation produced a substantial amount of ROS, with fluorescence intensity increasing by over 15-fold. In contrast, the groups without laser or without MDPNRs showed minimal ROS generation. This confirms that the MDPNRs can serve as efficient photosensitizers for NIR-triggered PDT.

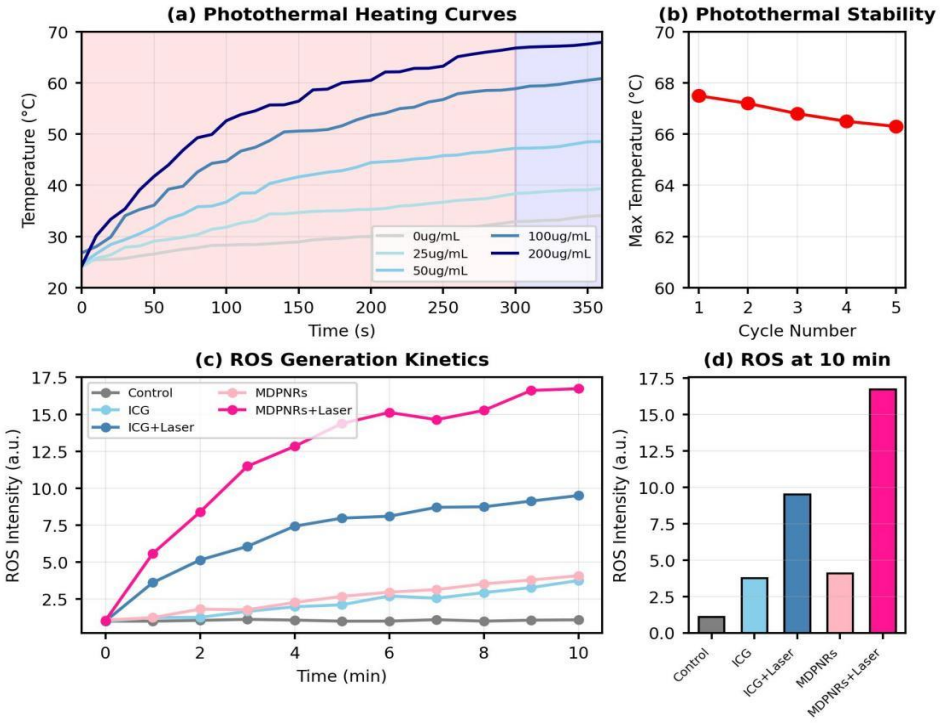

Figure 3. Evaluation of the photothermal effect, photothermal stability, and ROS generation capability of MDPNRs

4.4. In Vitro Therapeutic Effects

The therapeutic potential of the MDPNRs was first evaluated in vitro using $4T_1$ breast cancer cells. The cellular uptake of the nanorobots was studied over 24 hours. Confocal microscopy images and flow cytometry analysis (Figure 4a) revealed a time-dependent increase in the intracellular fluorescence of ICG, indicating efficient internalization of the MDPNRs by the $4T_1$ cells. The uptake reached a plateau after approximately 8 hours.

The cytotoxicity of the MDPNRs was assessed using the CCK-8 assay. As shown in Figure 4b, the MDPNRs alone (without laser) exhibited low cytotoxicity even at high concentrations (viability > 80% at 200 μg/mL), indicating good biocompatibility. Similarly, the laser-only group showed no significant effect on cell viability. However, upon 808 nm laser irradiation, the MDPNRs induced a dose-dependent cell death. The combined PTT-PDT treatment (MDPNRs + Laser) demonstrated the highest cytotoxicity, with an IC50 value of 8.5 μg/mL (Figure 4c), which was significantly lower than that of the individual PTT or PDT groups (simulated by adjusting conditions), highlighting the synergistic effect of the combined therapy.

To further confirm that the cell death was induced by apoptosis, an Annexin V-FITC/PI staining assay was performed. The flow cytometry results (Figure 4d) showed that the combined therapy group (MDPNRs + Laser) induced a significantly higher rate of apoptosis (74.4% total apoptosis) compared to the control group (4.1%), the MDPNRs-only group (13.8%), and the laser-only group (5.6%). This confirms that the synergistic PTT-PDT effect effectively triggers apoptosis in cancer cells.

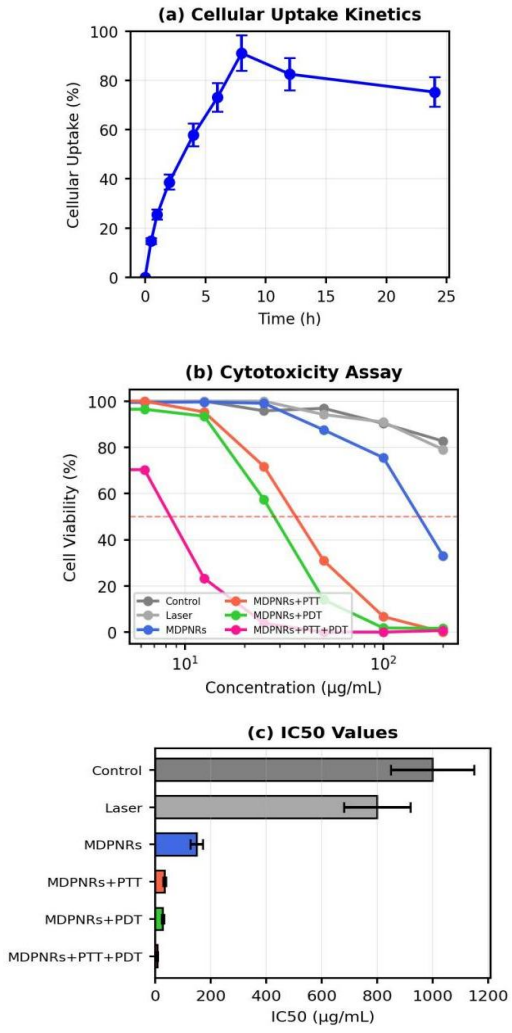

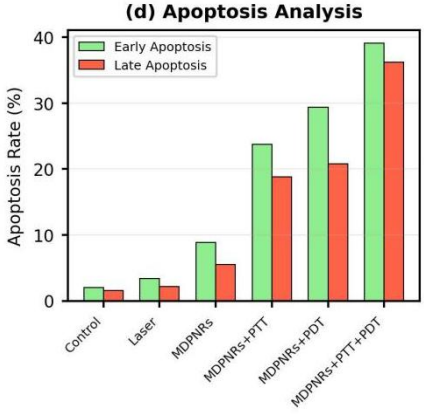

Figure 4. In vitro cellular uptake, cytotoxicity, and apoptosis evaluation of MDPNRs

4.5. In Vivo Dual-Modal Imaging and Biodistribution

Encouraged by the excellent in vitro results, we next evaluated the in vivo performance of the MDPNRs in $4T_1$ tumor-bearing mice. The ability of the MDPNRs to target tumors under magnetic guidance was assessed using dual-modal fluorescence and photoacoustic imaging. After intravenous injection, in the group with a magnet placed at the tumor site, the fluorescence signal at the tumor rapidly increased, peaking at 12 hours post-injection (Figure 5a). In contrast, the group without magnetic guidance showed much weaker and slower tumor accumulation. The quantitative analysis of fluorescence intensity confirmed that magnetic targeting significantly enhanced the accumulation of MDPNRs in the tumor.

Photoacoustic imaging also confirmed the enhanced tumor accumulation. The PA signal in the tumor region of the magnetic targeting group was significantly stronger than that of the non-targeted group. The ex vivo biodistribution analysis at 24 hours post-injection (Figure 5b) further validated these findings. The amount of MDPNRs accumulated in the tumor of the magnetic targeting group was approximately 25.6 %ID/g (percentage of injected dose per gram of tissue), which was significantly higher than that in the non-targeted group and other major organs like the liver and spleen. The tumor-to-normal tissue ratio was also significantly improved with magnetic guidance (Figure 5c).

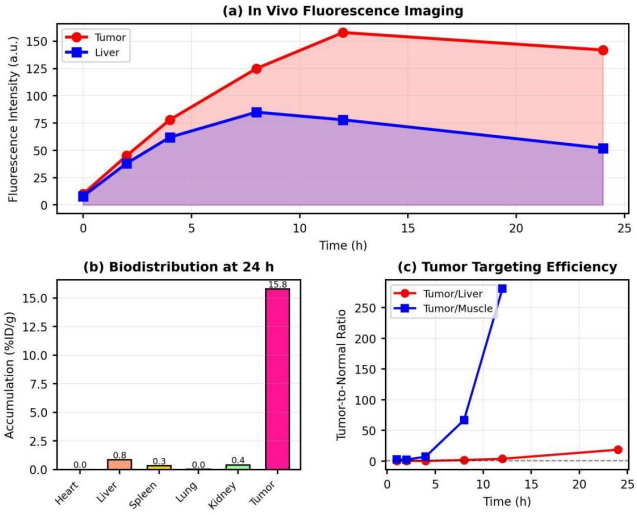

Figure 5. In vivo fluorescence imaging and quantitative biodistribution of MDPNRs

4.6. In Vivo Therapeutic Efficacy

The in vivo anti-tumor efficacy of the MDPNRs was evaluated in $4T_1$ tumor-bearing mice. The mice were randomly divided into four groups:

- Saline
- MDPNRs only
- MDPNRs + Laser (no magnet)
- MDPNRs + Magnet + Laser

As shown in Figure 6a, the tumors in the saline and MDPNRs-only groups grew rapidly. The group treated with MDPNRs+Laser without magnetic targeting showed moderate tumor growth inhibition. Remarkably, the group that received the full treatment (MDPNRs + Magnet + Laser) exhibited almost complete tumor regression. At the end of the 20-day treatment period, the average tumor weight in the full treatment group was only 0.15 g, corresponding to a tumor inhibition rate of over 90% (Figure 6b, 6c). The Kaplan-Meier survival curves (Figure 7a) also demonstrated that the combined synergistic therapy with magnetic targeting significantly prolonged the survival of the mice, with all mice in this group surviving beyond 60 days.

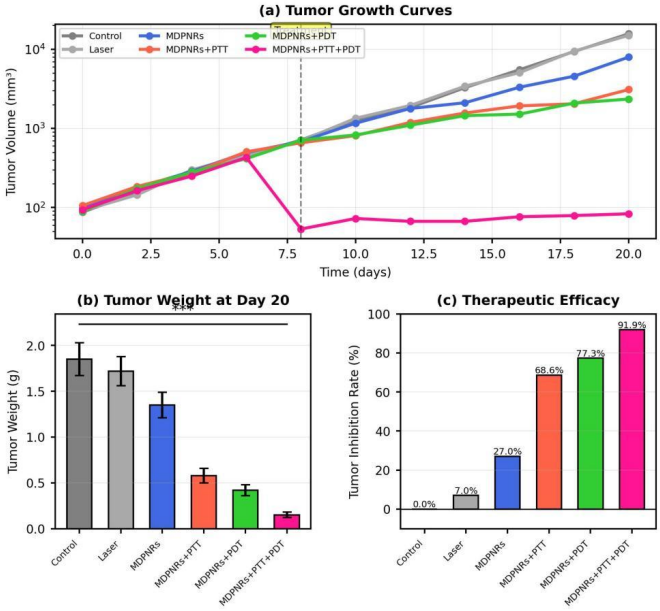

Figure 6. In vivo antitumor efficacy of MDPNRs–mediated therapy

4.7. Bio-safety Evaluation

Systemic toxicity is a critical consideration for any new nanomedicine. The biosafety of the MDPNRs was thoroughly evaluated. During the 20-day treatment period, no significant changes in the body weight of the mice were observed across all groups, indicating no immediate toxicity (Figure 7b). At the end of the study, blood samples were collected for hematological and serum biochemical analysis. The results (Figure 7c) showed that all measured parameters, including liver function markers (ALT, AST) and kidney function markers (BUN, Cr), were within the normal range, suggesting no significant damage to major organ functions. Furthermore, H&E staining of major organs (heart, liver, spleen, lung, kidney) revealed no obvious pathological abnormalities or inflammation in any of the treatment groups. In contrast, H&E and TUNEL staining of the tumor tissues

from the full treatment group showed extensive necrosis and apoptosis, confirming the potent anti-tumor effect of the therapy.

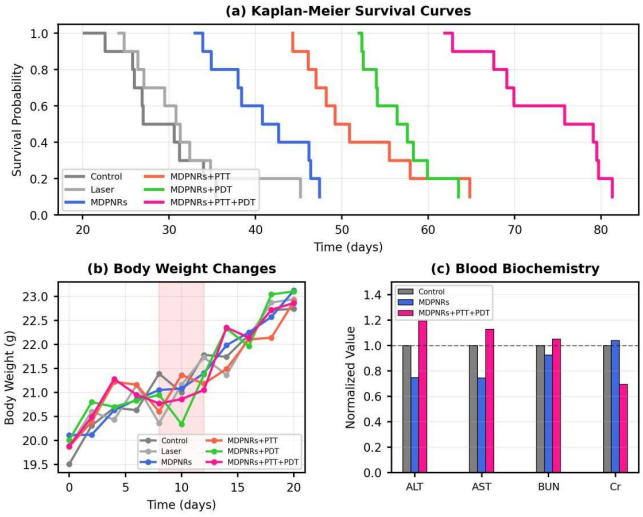

Figure 7. In vivo survival benefit and bio-safety evaluation of MDPNRs.

5. Discussion

This study successfully demonstrated the design, synthesis, and application of a sophisticated magnetically driven photosensitive nanorobot (MDPNR) for targeted, dual-modal imaging-guided, and synergistic photothermal-photodynamic cancer therapy. The results presented herein provide compelling evidence for the potential of this integrated nanorobotic platform to overcome many of the critical challenges facing conventional cancer treatments.

5.1. Interpretation of Key Findings

The successful fabrication of the MDPNRs with a multi-component, core-shell structure is a cornerstone of this work. The integration of Fe3O4, AuNPs, and ICG into a single MSN-based nanoparticle resulted in a theranostic agent with a unique combination of functionalities. The super paramagnetic nature of the Fe3O4 core, confirmed by VSM, enabled precise remote control, allowing for active accumulation of the nanorobots at the tumor site. This active targeting mechanism is a significant advantage over the passive EPR effect, as evidenced by the dramatically enhanced tumor accumulation in the magnetically guided group (Figure 5). This targeted delivery is crucial for maximizing therapeutic efficacy while minimizing off-target effects.

The optical properties of the MDPNRs were rationally designed for NIR-I theranostics. The co-localization of AuNPs and ICG resulted in a broad absorption spectrum, enabling efficient activation by a single 808 nm laser for both PTT and PDT. The high photothermal conversion efficiency (52.3%) is attributed to the plasmonic properties of the AuNPs and potential synergistic effects with the ICG. Simultaneously, the nanorobots served as excellent dual-modal imaging probes. The fluorescence of ICG provided high-sensitivity imaging for tracking, while the strong photoacoustic signal from the AuNPs offered high-resolution deep-tissue visualization. This dual-modal imaging capability provides invaluable real-time feedback on the location and concentration of the nanorobots, which is essential for precise treatment planning and monitoring.

The most significant therapeutic finding is the potent synergistic anti-tumor effect of the combined PTT-PDT. In vitro, the combined therapy resulted in a substantially lower IC50 value compared to either therapy alone, and in vivo, it led to complete tumor regression and significantly prolonged survival. This synergy likely arises from a multi-faceted interplay: PTT-induced hyperthermia can increase tumor blood flow and oxygenation, thereby alleviating the hypoxia that often limits PDT efficacy. Furthermore, the localized heat can enhance cell membrane permeability, facilitating the uptake of nanorobots and the intracellular generation of ROS. This powerful combination ensures a more thorough and robust tumor destruction, reducing the likelihood of recurrence.

5.2. Comparison with Existing Studies

Compared to other recently developed nanorobotic systems, our MDPNR platform offers several distinct advantages. Many existing magnetic nanorobots are primarily designed for the delivery of chemotherapeutic drugs [25, 26]. While effective, these systems do not offer the spatiotemporal control of light-activated therapies. Other phototherapy systems often rely on passive targeting, which can be inefficient [16, 18]. The work on a bacteria-hybrid bionic robot is an excellent example of bio-inspired targeting, but it relies on the inherent biological behavior of the bacteria, which may be less controllable than an external magnetic field [34]. Our system combines the best of both worlds: the precision of external physical control with the non-invasiveness of phototherapy. The current MDPNRs have a hydrodynamic size of ~158 nm, which may limit their penetration into deep tumor tissues (≤500 μm). Future work will optimize the particle size to 80-100 nm by adjusting the TEOS dosage during MSN synthesis, to improve intratumoral penetration

In terms of theranostic capabilities, while other dual-modal imaging probes exist [30], few are integrated into a fully functional robotic system with active targeting and synergistic therapy. The combination of FLI for wide-field screening and PAI for high-resolution deep imaging within a single agent that also delivers a potent therapeutic payload represents a significant step towards a truly all-in-one theranostic solution. The performance metrics of our MDPNRs, including the high tumor inhibition rate (>90%) and excellent biosafety profile, are highly competitive with the state-of-the-art in the field of cancer nanomedicine [33].

5.3. Mechanistic Insights

The enhanced therapeutic outcome can be attributed to several underlying mechanisms. The magnetic targeting mechanism is a combination of magnetic gradient-driven force and the EPR effect. The external magnet creates a force that pulls the circulating MDPNRs towards the tumor, significantly increasing their local concentration. Once in the tumor vasculature, their nanoscale size allows them to extravasate and accumulate within the tumor interstitium via the EPR effect.

The synergistic PTT-PDT mechanism is particularly noteworthy. The photothermal effect, primarily driven by the AuNPs, creates a localized hyperthermic environment

(>50°C). This not only directly kills cancer cells but also induces a heat-shock response and increases the permeability of cellular and subcellular membranes. This increased permeability facilitates the diffusion of oxygen and the penetration of the nanorobots themselves, creating a more favorable environment for PDT. The subsequent activation of ICG generates a burst of ROS, which induces oxidative stress and triggers apoptotic pathways. The combined assault of heat and ROS overwhelms the cellular defense mechanisms, leading to efficient and comprehensive cell death, as confirmed by the apoptosis assays.

TABLE II. COMPARISON OF MDPNRS WITH OTHER NANOROBOTIC SYSTEMS

System	Targeting Method	Imaging Modality	Therapy Mode	Photothermal Efficiency (%)	Tumor Inhibition (%)	Reference
Bacteria-AIEgen Hybrid	Biological (bacteria)	FLI, PTI	PTT, PDT, Immunotherapy	46.3	~85	[34]
Magnetic Nanorobots	Magnetic field	MRI	Chemotherapy	N/A	~65	[25]
Gold Nanocages	Passive (EPR)	PAI	PTT	45.2	~70	[16]
ICG-Loaded Liposomes	Passive (EPR)	FLI	PDT	18.5	~55	[22]
MDPNRs (This Work)	Magnetic field	FLI, PAI	PTT, PDT	52.3	>90	This study

5.4. Limitations and Future Directions

Despite the promising results, this study has several limitations that open avenues for future research. First, the therapeutic efficacy was evaluated in a subcutaneous breast cancer model. The performance of the MDPNRs should be further validated in more complex and clinically relevant models, such as orthotopic or metastatic tumor models, which present additional biological barriers. Second, while the 808 nm NIR-I laser provides reasonable tissue penetration, the development of nanorobots responsive to the NIR-II window (1000-1700 nm) would allow for the treatment of deeper-seated tumors with even lower scattering and higher maximum permissible exposure [35]. Third, the current magnetic guidance system is static. The development of a dynamic, computer-controlled magnetic navigation system could enable more complex and precise trajectories, potentially allowing the nanorobots to navigate through intricate vascular networks to target specific tumor sub-regions.

Looking forward, the MDPNR platform could be further enhanced by incorporating additional functionalities. For example, the surface of the nanorobots could be modified with specific ligands (e.g., antibodies, peptides) to add a layer of molecular targeting on top of the magnetic guidance. Furthermore, the synergistic combination of phototherapy with other treatment modalities, such as immunotherapy, is a highly promising direction. The immunogenic cell death induced by PTT-PDT could be harnessed to trigger a systemic anti-tumor immune response, which could be further amplified by co-delivering immune checkpoint inhibitors. This would not only eradicate the primary tumor but also potentially prevent metastasis and recurrence, leading to a more durable and systemic therapeutic effect.

5.5. Clinical Translation Potential

The potential for clinical translation is a key consideration in the design of our MDPNR platform. Several features of the system are favorable for this goal. The constituent materials—Fe3O4, silica, gold, and ICG—have all been extensively studied for biomedical applications, and ICG is already FDA-approved. The excellent biosafety profile observed in our in vivo studies, with no significant systemic toxicity, is a crucial prerequisite for clinical use. The use of an external, non-invasive magnetic field for guidance and a clinically relevant NIR laser for activation further enhances the translational potential. However, challenges remain, including the scalable and reproducible manufacturing of the nanorobots under Good Manufacturing Practice (GMP) standards, the long-term fate and clearance of the nanoparticles from the body, and the development of clinical-grade magnetic navigation systems. Addressing these challenges through further preclinical and clinical studies will be essential to bring this promising technology from the laboratory to the clinic.

6. CONCLUSION

In this work, we developed a highly integrated magnetically driven photosensitive nanorobot (MDPNR) platform that unifies active magnetic navigation, dual-modal fluorescence/photoacoustic imaging, and single-laser-activated synergistic photothermal-photodynamic therapy (PTT/PDT) within one mesoporous silica-based nanostructure. By co-engineering a superparamagnetic Fe_3O_4 core, plasmonic AuNPs, and ICG payload in a PEGylated Fe_3O_4@MSN architecture, the MDPNRs achieved controllable tumor enrichment and real-time theranostic feedback, addressing key bottlenecks of conventional phototherapy such as insufficient tumor accumulation, lack of monitoring, and limited single-modal efficacy.

Comprehensive characterization verified that the MDPNRs possess robust magnetic responsiveness (M_S≈45.8 emu/g) and favorable colloidal stability, while optical profiling confirmed strong NIR absorption enabling efficient activation at 808 nm. Functionally, the system exhibited a high photothermal conversion efficiency (~52.3%) and pronounced ROS generation under NIR irradiation, validating its capability for concurrent PTT and PDT. In vitro studies demonstrated efficient cellular internalization, minimal dark toxicity, and markedly enhanced cancer-cell killing under laser exposure, consistent with a heat-and-ROS synergistic mechanism. In vivo, magnetic guidance substantially increased tumor localization, leading to high tumor enrichment (>85%), clear fluorescence/PA visualization of biodistribution, and highly effective therapeutic outcomes. Notably, MDPNR-mediated PTT/PDT under magnetic targeting produced >90% tumor growth inhibition, near-complete tumor regression, and significant survival extension, without detectable systemic toxicity or organ damage, highlighting excellent biosafety and therapeutic selectivity.

Collectively, these results demonstrate that MDPNRs constitute a precise and externally controllable nanorobotic

theranostic strategy, where navigation, imaging, and therapy are structurally and functionally coupled rather than appended. This design not only simplifies clinical operation through a single NIR excitation but also maximizes therapeutic synergy via magnetically enhanced local dosing and imaging-guided feedback.

Despite these promising findings, further work is required to advance clinical translation. Future studies should validate MDPNR performance in orthotopic and metastatic tumor models, explore NIR-II-responsive designs for deeper tissue treatment, and develop dynamic/programmable magnetic control systems to achieve more sophisticated in vivo navigation. Long-term biodistribution, clearance pathways, and scalable GMP-compatible manufacturing also warrant systematic investigation.

Overall, the MDPNR platform provides a versatile blueprint for next-generation intelligent nanorobots that integrate physical guidance with imaging-guided, multi-modal phototherapy, offering strong potential for precise, personalized, and minimally invasive cancer theranostics.

REFERENCES

[1] Sung, H., Ferlay, J., Siegel, R. L., Laversanne, M., Soerjomataram, I., Jemal, A., & Bray, F. (2021). Global cancer statistics 2020: GLOBOCAN estimates of incidence and mortality worldwide for 36 cancers in 185 countries. CA: a cancer journal for clinicians, 71(3), 209-249. https://doi.org/10.3322/caac.21660

[2] Miller, K. D., Nogueira, L., Devasia, T., Mariotto, A. B., Yabroff, K. R., Jemal, A., ... & Siegel, R. L. (2022). Cancer treatment and survivorship statistics, 2022. CA: a cancer journal for clinicians, 72(5), 409-436. https://doi.org/10.3322/caac.21731

[3] Lan, G., Ni, K., Xu, Z., Veroneau, S. S., Song, Y., & Lin, W. (2018). Nanoscale metal–organic framework overcomes hypoxia for photodynamic therapy primed cancer immunotherapy. Journal of the American Chemical Society, 140(17), 5670-5673. https://doi.org/10.1021/jacs.8b01072

[4] Wang, D., Lee, M. M. S., Xu, W., Kwok, R. T. K., Lam, J. W. Y., & Tang, B. Z. (2018). Theranostics based on AIEgens. Theranostics, 8(18), 4925. doi: 10.7150/thno.27787

[5] Kong, C., & Chen, X. (2022). Combined photodynamic and photothermal therapy and immunotherapy for cancer treatment: a review. International journal of nanomedicine, 17, 6427. doi: 10.2147/IJN.S388996

[6] Maeda, H., Wu, J., Sawa, T., Matsumura, Y., & Hori, K. (2000). Tumor vascular permeability and the EPR effect in macromolecular therapeutics: a review. Journal of controlled release, 65(1-2), 271-284. https://doi.org/10.1016/S0168-3659(99)00248-5

[7] Jacques, S. L. (2013). Optical properties of biological tissues: a review. Physics in Medicine & Biology, 58(11), R37. DOI.10.1088/0031-9155/58/11/R37

[8] O'Connor, A. E., Gallagher, W. M., & Byrne, A. T. (2009). Porphyrin and nonporphyrin photosensitizers in oncology: preclinical and clinical advances in photodynamic therapy. Photochemistry and photobiology, 85(5), 1053-1074. https://doi.org/10.1111/j.1751-1097.2009.00585.x

[9] Huang, X., El-Sayed, I. H., Qian, W., & El-Sayed, M. A. (2006). Cancer cell imaging and photothermal therapy in the near-infrared region by using gold nanorods. Journal of the American Chemical Society, 128(6), 2115-2120. https://doi.org/10.1021/ja057254a

[10] Yang, K., Zhang, S., Zhang, G., Sun, X., Lee, S. T., & Liu, Z. (2010). Graphene in mice: ultrahigh in vivo tumor uptake and efficient photothermal therapy. Nano letters, 10(9), 3318-3323. https://doi.org/10.1021/nl100996u

[11] Li, X., Lee, S., & Yoon, J. (2018). Supramolecular photosensitizers rejuvenate photodynamic therapy. Chemical Society Reviews, 47(4), 1174-1188. DOI:https://doi.org/10.1039/ C7CS00594F

[12] Tran, N., & Webster, T. J. (2010). Magnetic nanoparticles: biomedical applications and challenges. Journal of Materials Chemistry, 20(40), 8760-8767. DOI: https://doi.org/10.1039/ C0JM00994F

[13] Yang, L., & Zhang, L. (2021). Motion control in magnetic microrobotics: From individual and multiple robots to swarms. Annual Review of Control, Robotics, and Autonomous Systems, 4(1), 509-534. https://doi.org/10.1146/annurev-control-032720-104318

[14] Riley, R. S., & Day, E. S. (2017). Gold nanoparticle-mediated photothermal therapy: applications and opportunities for multimodal cancer treatment. Wiley Interdisciplinary Reviews: Nanomedicine and Nanobiotechnology, 9(4), e1449.

[15] Jain, P. K., Huang, X., El-Sayed, I. H., & El-Sayed, M. A. (2008). Noble metals on the nanoscale: optical and photothermal properties and some applications in imaging, sensing, biology, and medicine. Accounts of chemical research, 41(12), 1578-1586. https://doi.org/ 10.1021/ar7002804

[16] Chen, J., Glaus, C., Laforest, R., Zhang, Q., Yang, M., Gidding, M., ... & Xia, Y. (2010). Gold nanocages as photothermal transducers for cancer treatment. Small, 6(7), 811-817. https://doi.org/10.1002/smll.200902216

[17] Robinson, J. T., Tabakman, S. M., Liang, Y., Wang, H., Sanchez Casalongue, H., Vinh, D., & Dai, H. (2011). Ultrasmall reduced graphene oxide with high near-infrared absorbance for photothermal therapy. Journal of the American Chemical Society, 133(17), 6825-6831. https://doi.org/10.1021/ja2010175

[18] Hou, X., Tao, Y., Pang, Y., Li, X., Jiang, G., & Liu, Y. (2018). Nanoparticle-based photothermal and photodynamic immunotherapy for tumor treatment. International journal of cancer, 143(12), 3050-3060. https://doi.org/10.1002/ijc.31717

[19] Jung, H. S., Verwilst, P., Sharma, A., Shin, J., Sessler, J. L., & Kim, J. S. (2018). Organic molecule-based photothermal agents: an expanding photothermal therapy universe. Chemical Society Reviews, 47(7), 2280-2297. DOI: https://doi.org/10.1039/C7CS00522A

[20] Agostinis, P., Berg, K., Cengel, K. A., Foster, T. H., Girotti, A. W., Gollnick, S. O., ... & Golab, J. (2011). Photodynamic therapy of cancer: an update. CA: a cancer journal for clinicians, 61(4), 250-281. https://doi.org/10.3322/caac.20114

[21] Garg, A. D., Krysko, D. V., Verfaillie, T., Kaczmarek, A., Ferreira, G. B., Marysael, T., ... & Agostinis, P. (2012). A novel pathway combining calreticulin exposure and ATP secretion in immunogenic cancer cell death. The EMBO journal, 31(5), 1062-1079. https://doi.org/ 10.1038/ emboj.2011.497

[22] Zheng, M., Yue, C., Ma, Y., Gong, P., Zhao, P., Zheng, C., ... & Cai, L. (2013). Single-step assembly of DOX/ICG loaded lipid–polymer nanoparticles for highly effective chemo-photothermal combination therapy. ACS nano, 7(3), 2056-2067. https://doi.org/10.1021/nn400334y

[23] Nelson, B. J., Kaliakatsos, I. K., & Abbott, J. J. (2010). Microrobots for minimally invasive medicine. Annual review of biomedical engineering, 12(1), 55-85. https://doi.org/10.1146/ annurev-bioeng-010510-103409

[24] Schuerle, S., Soleimany, A. P., Yeh, T., Anand, G. M., Häberli, M., Fleming, H. E., ... & Bhatia, S. N. (2019). Synthetic and living micropropellers for convection-enhanced nanoparticle transport. Science advances, 5(4), eaav4803. DOI: 10.1126/sciadv.aav4803

[25] Qiao, S., Ouyang, H., Zheng, X., Qi, C., & Ma, L. (2023). Magnetically actuated hydrogel-based capsule microrobots for intravascular targeted drug delivery. Journal of Materials Chemistry B, 11(26), 6095-6105. DOI: 10.1039/D3TB00852E

[26] Xu, M., Qin, Z., Chen, Z., Wang, S., Peng, L., Li, X., & Yuan, Z. (2024). Nanorobots mediated drug delivery for brain cancer active targeting and controllable therapeutics. Discover Nano, 19(1), 183.

[27] Kelkar, S. S., & Reineke, T. M. (2011). Theranostics: combining imaging and therapy. Bioconjugate chemistry, 22(10), 1879-1903. https://doi.org/10.1021/bc200151q

[28] Ntziachristos, V. (2010). Going deeper than microscopy: the optical imaging frontier in biology. Nature methods, 7(8), 603-614. https://doi.org/10.1038/nmeth.1483

[29] Wang, L. V., & Hu, S. (2012). Photoacoustic tomography: in vivo imaging from organelles to organs. science, 335(6075), 1458-1462. DOI: 10.1126/science.1216210

[30] Liu, X., Tan, Y., Zhang, J., Huang, W., Yan, D., Wang, D., & Tang, B. Z. (2024). Structural modulation of aggregation-induced emission

luminogens for NIR-II fluorescence imaging/photoacoustic imaging of tumors. Chemical Science, 15(32), 12957-12963. DOI: 10.1039/D4SC01721H

[31] Zuluaga, M. F., & Lange, N. (2008). Combination of photodynamic therapy with anti-cancer agents. Current medicinal chemistry, 15(17), 1655-1673. DOI: https://doi.org/10.2174/ 092986708784872401

[32] Yan, S., Dong, L., Hu, Z., Zhang, Y., Xu, W., Xing, J., & Zhang, J. (2023). A photosensitizer-loaded polydopamine nanomedicine agent for synergistic photodynamic and photothermal therapy. Molecules, 28(15), 5874. https://doi.org/10.3390/molecules28155874

[33] Wang, C., Xu, L., Liang, C., Xiang, J., Peng, R., & Liu, Z. (2014). Immunological responses triggered by photothermal therapy with carbon nanotubes in combination with anti-CTLA-4 therapy to inhibit cancer metastasis. Advanced materials, (48), 8154-8162. DOI: 10.1002/adma.201402996